This is a repository copy of *Stimulated Transitions of Directed Nonequilibrium Self-Assemblies*.

White Rose Research Online URL for this paper:
http://eprints.whiterose.ac.uk/122982/

Version: Supplemental Material

WILEY-VCH

Supporting Information

Stimulated Transitions of Directed Non-Equilibrium Self-Assemblies

Alexander A. Steinschulte, Andrea Scotti, Khosrow Rahimi, Oleksii Nevskyi, Alex Oppermann, Sabine Schneider, Steffen Bochenek, Marie F. Schulte, Karen Geisel, Felicitas Jansen, Andre Jung, Sabrina Mallmann, Roland Winter, Walter Richtering, Dominik Wöll, Ralf Schweins, Nicholas J. Warren,* Felix A. Plamper*

Materials.

N-isopropyl acrylamide (NIPAM), *tert*-butyl acrylamide (tBAM), 4,4′-azobis(4-cyanovaleric acid (ACVA), *N,N*-dimethyl acrylamide (DMAM), ethanol, diethyl ether, 2-phenylethanethiol, potassium triphosphate, carbon disulfide, 2-bromo-2-methylpropionic, *N*-hydroxysuccinimid (NHS), *N*-(3-dimethylaminopropyl)-*N`*-ethylcarbodiimide hydrochloride (EDC), β-mercaptoethylamine (MEA), magnesium sulfate, ethyl acetate and hexane were delivered by Sigma Aldrich. D_2O was obtained by Deutero GmbH. 4-(2-Hydroxyethyl)piperazine-1-ethanesulfonic acid (HEPES) was obtained from VWR. Alexa Fluor 647 Cadaverine was obtained from ThermoFisher Scientific.

Synthesis of 2-(phenylethylthiocarbonothioylthio)-2-methylpropanoic acid (PETAc).

10.0 g (72.5 mmol) of 2-phenylethanethiol and 32.1 g (144.9 mmol) of potassium triphosphate were added to 200 mL of acetone. After 30 minutes of vigorous stirring, 13.8 g (181.2 mmol) of carbon disulfide was added to the suspension. The reaction mixture was stirred for 1 hour and 13.3 g (79.7 mmol) of 2-bromo-2-methylpropionic acid were added dropwise and the reaction mixture was stirred at 20 °C for 30 hours. The reaction mixture was then filtered and acetone was removed under vacuum. The residual oil was dissolved in diethyl ether (200 mL) and this solution was washed twice with 200 mL of 10 % HCl aqueous solution and 3 times with 200 mL of deionized water. The ether phase was dried with magnesium sulfate and the ether was removed under vacuum. The crude product recrystallized from ethyl acetate:hexane 1:10 v:v. 15.1 g (50.25 mmol) of pure RAFT agent were obtained. Yield = 69 %
^{1}H NMR (400.13 MHz, CDCl$_3$, 298 K) δ (ppm): 1.72 (6H, CH$_3$), 2.91-2.97 (t, 2H, SCH$_2$CH$_2$Ph), 3.47-3.54 (t, 2H, SCH$_2$CH$_2$Ph), 7.18-7.31 (m, 5H, Ph).
^{13}C NMR (400.13 MHz, CD$_2$Cl$_2$, 298 K) δ (ppm): 25.3 (C*H*$_3$), 34.3 (C*H*$_2$Ph), 38.1 (SC*H*$_2$CH$_2$Ph), 55.8 (C(CH$_3$)$_2$), 126.8, 128.7, 139.6 (Ph), 179.3 (C=O), 220.4 (C=S).

Synthesis of the PDMAM$_{49}$ Macro CTA.

20.01 g of the monomer dimethyl acrylamide (0.2020 mol, 49 eq), 1.354 g of the CTA 2-(phenylethylthiocarbonothioylthio)-2-methylpropanoic acid (0.00412 mol; 1 eq) (for more information see scheme in Main Part) and 0.1157 g of the initiator 4,4′-azobis(4-cyanovaleric acid) (0.000412; 0.1 eq) (ACVA) were added to a round-bottomed flask. To this mixture 30 g (leading to ~60 wt% solvent) degassed ethanol (bubbled with N$_2$ over night) was added. The mixture was cooled with an ice bath and purged with N$_2$ for 30 min. To start the reaction the sealed flask was immersed into an oil bath set at 70 °C. After 35 min the reaction was stopped by quenching in an ice bath and adding 30 ml of non-degassed methanol (90 % conversion according to NMR). The polymer was purified by precipitation in excess of diethyl ether. Finally, the precipitate was dissolved in water and freeze-dried to yield 17 g of polymer.
In order to preserve the RAFT end-group of the PDMAM, the polymerization was quenched before full conversion at 90% DMAM conversion. A single large batch (17 g) of the PDMAM macro-CTA was produced to ensure precisely the same actual degree of polymerization (and blocking efficiency).[1]
SEC (DMF, 1 g/L, PMMA calibration): M_n = 5.1 kg/mol, Đ= 1.16
^{1}H NMR (400.13 MHz, CDCl$_3$, 298 K) δ (ppm): 1.1-1.7 (2H, CH$_2$), 2.3-2.7 (m, 1H, CH$_2$-C*H*-CON), 2.7-3.2 (m, 6H, N-(C*H*$_3$)$_2$), 7.18-7.31 (m, 5H, Ph).

A typical protocol for the synthesis of PDMAM$_{49}$-*b*-P(NIPAM-*st*-tBAM)$_x$ is as follows.

0.3138 g of the monomer NIPAM (0.00278 mol; 131 eq), 0.1861 g of the monomer tBAM (0.00146 mol 69 eq), 0.1097 g of the macro CTA PDMAM$_{49}$ (0.0212 mmol; 1 eq) and 0.0020 g (0.0071 mmol; 0.33 eq) of the initiator 4,4′-azobis(4-cyanovaleric acid) (ACVA) were added to a vial. To this mixture, 2.435 g degassed water (purged with N$_2$ over night) was added. The mixture was cooled with an ice bath and bubbled with N$_2$ for 30 min. To start the reaction, the sealed flask was immersed into an oil bath set at 70 °C. After 2 h the reaction was stopped by cooling to 25 °C and purging with pressurized air (99 % conversion according to NMR). Reaction mixture was used without further purification.

SEC (DMF, 1 g/L, PMMA calibration): M_w = 42.7 kg/mol, $Đ$= 1.2

^{1}H NMR (400.13 MHz, CD$_3$OD, 298 K) δ (ppm): 1.0-1.9 (N-CH-(C*H$_3$*)$_2$, N-C-(C*H$_3$*)$_3$), 1.9-2.3 (2H, C*H$_2$*), 2.4-2.85 (m, 1H, CH$_2$-C*H*-CON), 2.85-3.25 (m, 6H, N-(C*H$_3$*)$_2$) 3.8-4.1 (bs, 1H, N*H*), 7.1-7.4 (m, 5H, Ph).

Fluorescence labeling.

Labeling of the gel-forming A$_{49}$-*b*-B$_{400}$-S50 with Alexa Fluor 647 dye was achieved by following procedure. About 100 µL of micellar sample of pristine A$_{49}$-*b*-B$_{400}$-S50 (~50 g/L; 10^{-7} mol carboxy groups) was cooled for 2 h at 4 °C to activate the gel formation on a glass cover slide upon return to room temperature (by shortly placing the cooled sample for 1 min at 60 °C). The gel was incubated for 1 day with several drops of a labeling buffer (0.5 mg NHS, 1 mg of EDC and 120 mg of HEPES in 10 mL water, then adjusted to pH 7 by addition of 0.1 M NaOH/HCl; incubation took place in a closed, wetted petri-dish to avoid evaporation of water). Then, residual incubation buffer was removed carefully from the gel with a tissue and approximately 20 µL of a fluorescence dye solution of Alexa Fluor 647 Cadaverine (i.e. 2 · 10^{-8} mol amino/dye groups; obtained after mixing 5 µL a 5mM dye solution in DMSO with 20 µL of the labeling buffer) was placed on top of the gel. To enhance the labeling efficiency, a tip of a spatula NHS (~1 mg) and EDC (~ 5 mg) was added on top for dissolution and equilibration overnight (again in a closed petri-dish). Subsequent purification was achieved by placing carefully several drops of labeling buffer on top of the labeled gel with repeated replacement of the drops with fresh buffer ("dialysis" for two days). For complete homogeneous labeling, the gel was reactivated by applying another cooling and heating cycle (after residual excess buffer was carefully removed with tissue).

^{1}H NMR Spectroscopy.

All NMR spectra were recorded using a 400 MHz Bruker Avance-400 spectrometer (64 scans averaged per spectrum) at RT using either CDCl$_3$, D$_2$O, or CD$_3$OD.

Gel Permeation Chromatography (GPC).

The molecular weights and dispersities of copolymers synthesized in H$_2$O were determined using a DMF GPC setup operated at 60 °C and comprising two Polymer Laboratories PL gel 5 µm Mixed-C columns connected in series to a Varian 390-LC multidetector suite (refractive index detector only) and a Varian 290-LC pump injection module. The GPC eluent was HPLC grade DMF containing 10 mM LiBr at a flow rate of 1.0 mL min^{-1}. DMSO was used as a flow-rate marker. Calibration was conducted using a series of near-monodisperse poly(methyl methacrylate) standards (M_n= 625−618 000 g mol^{-1}). Chromatograms were analyzed using Varian CirrusGPC software (version 3.3).

The samples synthesized in D$_2$O were analyzed in the following GPC setup. The analyses were performed at room temperature using a high-pressure liquid chromatography pump (Bischoff 2250) and a refractive index detector (Jasco 2031plus). The eluting solvent was dimethylformamide (DMF) with 1 g/L LiBr and a flow rate of 1.0 mL/min. Five columns with

PSS GRAM material were applied. The length of the precolumn was 50 mm and the diameter 8 mm (30 Å). The remaining four columns had a length of 300 mm, diameter of 8 mm, particle size of 10 µm, and the nominal pore widths were 30, 100, 1000 and 3000 Å. Narrow-dispersed poly(methyl methacrylate) samples (PSS, Mainz, Germany) were used for (universal) calibration and the software package PSS WinGPC Unity (PSS, Mainz, Germany) was used for the evaluation.

Table S1. Polymer characterization

Exp. Nr.:[a]	Conversion (NIPAM)[c] [%]	DP (NIPAM)[d]	Conversion (tBAM)[c] [%]	DP (tBAM)[d]	Ratio NIPAM	M_w[e] [kg/mol]	M_w/M_n[e]
A$_{49}$-b-B$_{50}$-S50	98.2	32	98.4	17	0.66	13	1.2
A$_{49}$-b-B$_{50}$-S50[b]	96.3	31	95.9	16	0.66	11	1.1
A$_{49}$-b-B$_{75}$-S50	98.8	49	98.3	26	0.66	19	1.2
A$_{49}$-b-B$_{100}$-S50	98.6	64	99.0	34	0.65	24	1.3
A$_{49}$-b-B$_{90}$-S50[b]	95.8	57	97.8	30	0.66	17	1.2
A$_{49}$-b-B$_{150}$-S50	99.1	97	99.4	51	0.65	37	1.3
A$_{49}$-b-B$_{200}$-S50	99.2	130	99.6	68	0.66	46	1.3
A$_{49}$-b-B$_{250}$-S50	98.9	163	99.3	86	0.65	56	1.3
A$_{49}$-b-B$_{290}$-S50	96.4	189	99.6	103	0.65	60	1.3
A$_{49}$-b-B$_{400}$-S50	98.8	265	99.8	140	0.65	73	1.4
A$_{49}$-b-B$_{400}$-S50[b]	98.8	260	98.3	131	0.66	78	1.4
A$_{49}$-b-B$_{490}$-S50	98.6	318	99.9	170	0.65	90	1.4
A$_{49}$-b-B$_{690}$-S50	98.7	450	99.7	240	0.65	120	1.4
A$_{49}$-b-B$_{930}$-S50	91.9	602	93.6	323	0.65	150	1.4
A$_{49}$-b-B$_{130}$-S75	99.4	82	99.8	44	0.65	30	1.2
A$_{49}$-b-B$_{150}$-S75	99.3	98	99.6	52	0.65	35	1.2
A$_{49}$-b-B$_{200}$-S75	99.1	130	99.9	69	0.65	47	1.3
A$_{49}$-b-B$_{50}$-S100	99.5	33	99.8	17	0.66	13	1.2
A$_{49}$-b-B$_{75}$-S100	99.5	49	99.7	26	0.65	19	1.2
A$_{49}$-b-B$_{100}$-S100	99.8	66	99.7	35	0.66	24	1.2
A$_{49}$-b-B$_{125}$-S100	99.5	81	99.6	43	0.66	30	1.2
A$_{49}$-b-B$_{150}$-S100	99.3	98	98.2	51	0.66	35	1.2
A$_{49}$-b-B$_{200}$-S100	99.8	132	99.8	69	0.66	48	1.3
A$_{49}$-b-B$_{250}$-S100	99.5	163	99.3	86	0.66	56	1.3
A$_{49}$-b-B$_{300}$-S100	99.7	194	99.9	102	0.66	62	1.3
A$_{49}$-b-B$_{400}$-S100	99.6	262	99.6	138	0.66	79	1.3
A$_{49}$-b-B$_{85}$-S125	99.6	56	99.9	29	0.65	21	1.2
A$_{49}$-b-B$_{100}$-S125	99.7	65	99.8	34	0.66	23	1.2
A$_{49}$-b-B$_{130}$-S125	99.1	84	98.9	44	0.66	30	1.2
A$_{49}$-b-B$_{200}$-S125	99.4	128	98.6	67	0.66	44	1.3
A$_{49}$-b-B$_{50}$-S150	99.3	33	99.3	18	0.65	13	1.2
A$_{49}$-b-B$_{65}$-S150	99.8	42	99.9	22	0.66	16	1.2
A$_{49}$-b-B$_{70}$-S150	99.2	45	99.1	24	0.65	17	1.2
A$_{49}$-b-B$_{75}$-S150	99.8	49	99.9	26	0.65	18	1.2

Exp. Nr.:[a]	Conversion (NIPAM)[c] [%]	DP (NIPAM)[d]	Conversion (tBAM)[c] [%]	DP (tBAM)[d]	Ratio NIPAM	M_w[e] [kg/mol]	M_w/M_n[e]
A$_{49}$-b-B$_{80}$-S150	99.3	52	99.3	27	0.66	20	1.2
A$_{49}$-b-B$_{85}$-S150	99.6	58	99.8	30	0.66	21	1.2
A$_{49}$-b-B$_{90}$-S150	99.3	59	99.6	31	0.65	23	1.2
A$_{49}$-b-B$_{95}$-S150	99.6	62	99.6	33	0.66	23	1.2
A$_{49}$-b-B$_{100}$-S150	99.5	65	98.3	34	0.66	24	1.2
A$_{49}$-b-B$_{125}$-S150	99.8	82	99.0	43	0.66	29	1.2
A$_{49}$-b-B$_{150}$-S150	99.6	100	98.6	52	0.66	37	1.3
A$_{49}$-b-B$_{175}$-S150	99.7	116	99.3	60	0.66	39	1.2
A$_{49}$-b-B$_{200}$-S150	99.7	130	98.9	68	0.66	43	1.2
A$_{49}$-b-B$_{250}$-S150	99.6	166	99.6	88	0.65	54	1.2
A$_{49}$-b-B$_{300}$-S150	99.7	197	99.3	103	0.66	60	1.2
A$_{49}$-b-B$_{400}$-S150	99.4	263	98.9	136	0.66	74	1.2
A$_{49}$-b-B$_{50}$-S200	99.7	33	98.9	17	0.66	13	1.2
A$_{49}$-b-B$_{65}$-S200	99.6	41	99.2	21	0.66	15	1.2
A$_{49}$-b-B$_{70}$-S200	98.9	45	97.6	24	0.66	18	1.2
A$_{49}$-b-B$_{75}$-S200	99.9	49	98.5	25	0.66	19	1.2
A$_{49}$-b-B$_{80}$-S200	99.0	52	98.5	27	0.66	21	1.2
A$_{49}$-b-B$_{85}$-S200	98.8	57	92.6	28	0.67	21	1.2
A$_{49}$-b-B$_{90}$-S200	99.8	59	99.8	31	0.66	22	1.2
A$_{49}$-b-B$_{95}$-S200	99.4	62	99.0	32	0.66	23	1.2
A$_{49}$-b-B$_{100}$-S200	99.3	66	93.8	33	0.67	24	1.2
A$_{49}$-b-B$_{125}$-S200	99.9	82	99.3	43	0.66	30	1.2
A$_{49}$-b-B$_{150}$-S200	99.8	99	99.5	52	0.65	34	1.2
A$_{49}$-b-B$_{170}$-S200	99.5	114	96.3	58	0.66	39	1.2
A$_{49}$-b-B$_{200}$-S200	99.9	131	99.0	68	0.66	43	1.2
A$_{49}$-b-B$_{250}$-S200	99.9	162	99.1	85	0.66	51	1.2
A$_{49}$-b-B$_{300}$-S200	99.5	196	95.3	99	0.66	60	1.2
A$_{49}$-b-B$_{400}$-S200	99.5	260	99.2	137	0.65	76	1.2
A$_{49}$-b-B$_{400}$-S200[b]	98.3	258	99.4	137	0.65	68	1.3
A$_{49}$-b-B$_{510}$-S200	99.5	335	99.3	172	0.66	93	1.2
A$_{49}$-b-B$_{600}$-S200	99.4	391	99.4	206	0.66	99	1.2
A$_{49}$-b-B$_{690}$-S200	99.1	451	99.3	239	0.65	110	1.2
A$_{49}$-b-B$_{1000}$-S200	99.8	655	99.5	344	0.66	140	1.2

[a] PDMAM$_{49}$-b-P(NIPAM-st-tBAM)$_{DP}$ samples abbreviated A$_{49}$-b-B$_{DP}$ (DP gives the degree of polymerization of the core forming block) synthesized at concentration given by the number after S which gives the solid concentration during the synthesis in g/L. Throughout the

6

manuscript, g/L is used for solid content per solvent without regarding the volume change due to the solid content. The samples used in the main manuscript are additionally labeled with green background for LSC (low synthesis concentration) and orange background for HSC (high synthesis concentration).

[b] Samples synthesized in D_2O.

[c] Conversion is determined by ^{1}H-NMR.

[d] Degree of polymerization is determined by ^{1}H-NMR.

[e] Determined by DMF-GPC using PMMA standards.

Transmission Electron Microscopy (TEM).

Aggregate solutions were diluted at 20 °C to generate 0.1 % w/w dispersions. Copper/palladium TEM grids (Agar Scientific, UK) were surface-coated in-house to yield a thin film of amorphous carbon. The grids were then treated with a plasma glow discharge for 30 s to create a hydrophilic surface. Each aqueous diblock copolymer dispersion (0.1 % w/w, 12μL) was placed onto a freshly treated grid for 1 min and then blotted with filter paper to remove excess solution. To stain the deposited nanoparticles, a 0.75% w/w aqueous solution of uranyl formate (9 μL; in some cases with uranyl acetate) was placed via micropipet on the sample-loaded grid for 20 s and then carefully blotted to remove excess stain. Each grid was then carefully dried using a vacuum hose. Imaging was performed either at 100 kV using a Phillips CM100 instrument equipped with a Gatan 1 k CCD camera or with a 120 kV ZEISS LibraTM 120 microscope.

Dynamic light scattering (DLS).

Aggregate solutions were diluted at 20 °C to generate ~ 0.1 % w/w dispersions. In some cases, the measurements were performed with a Malvern Zetasizer Nano instrument at 173° and 20 °C. In other cases (where indicated), we used an ALV 5000 E autocorrelator equipped with a red Laser (λ= 633 nm) at 20 °C at several angles from 20° to 150°. The time-resolved signal of two Single Photon Counting Modules (SPCM-CD2969; Perkin Elmer) was cross-correlated.

Rheology.

The storage modulus (G′) and loss modulus (G″) curves were determined using a Malvern Kinexus pro+ rheometer equipped with a Peltier heating/cooling plate. A cone-and-plate geometry (40 mm 1° aluminum cone) equipped with a solvent trap was used for the measurements. For the temperature sweep, an amplitude and a frequency sweep were conducted at each temperature. Each temperature was equilibrated for at least 5 min.

Superresolution Fluorescence Microscopy.

A custom-built fluorescence microscopy setup was used. The beam of a 640 nm laser (Cobolt, 100 mW) was expanded using a parabolic mirror beam expander (Thorlabs) and focused via a mirror through a 500 mm plano convex lens onto the back focal plane of an Olympus UAPON 100X OTIRF objective of an Olympus IX 83 inverse microscope. The mirror and lens are mounted on a translation stage to shift the laser beam sideways to enable objective based total internal reflection (TIR) illumination of the sample. The fluorescence light was collected by the same objective and imaged onto the chip of a high sensitive EMCCD camera (Andor iXON Ultra 897).

In order to perform superresolution direct stochastic optical reconstruction microscopy (dSTORM),[2] the structures were labeled with the procedure described above and few drops of 500 mM MEA (β-mercaptoethylamine) were added as an appropriate STORM buffer.

The 640 nm laser was used with an irradiation intensity of 4 kW cm^{-1} to generate movies of blinking single molecules with 60,000 frames with an integration time of 25 ms. The superresolved dSTORM images were obtained after analysis of the movies with the ImageJ plugin ThunderSTORM[3] and the software ViSP.[4] The image was created by generating a Gaussian function for each localization using a 30 nm FWHM. The grayscale of the Gaussian function was scaled by the number of neighboring localizations within a radius of 100 nm.

Cryo-FE-SEM.

All measurements were performed on samples with a concentration of 50 g/L in D_2O. The samples were first cooled below their transition temperature and then heated to 25°C to form a gel. These gels were loaded onto rivet sample holders and frozen in liquid ethane for 5 min and transferred into liquid nitrogen. Hydrogel cross-sections were cut inside the FE-SEM pre-chamber and samples were visualized at 1kV and 1μA with FE-SEM SU4800 (Hitachi Ltd. Corporation) after 4 min sublimation at -80°C.

SANS[5].

SANS experiments were performed on the instrument D11 at the Institut Laue-Langevin (ILL, Grenoble, France). Measurements were performed either in a newly developed 5 kbar SANS high-pressure cell available at ILL or in 2 mm quartz cuvettes (for temperature dependent measurements). To cover the q-range of interest, $1.5 \cdot 10^{-3}$ Å^{-1} < q < $2.2 \cdot 10^{-1}$ Å^{-1}, we used a $\lambda = 6$ Å and $\Delta\lambda/\lambda = 9\%$ and three sample to detector distances: 3 m, 10 m and 39 m. For the quartz cuvette, the sample to detector distances of 1.2 m, 8 m and 39 m were used with the same λ, to cover a q-range between $1.5 \cdot 10^{-3}$ Å^{-1} < q < $4.2 \cdot 10^{-1}$ Å^{-1}.

Measurements with different pressure steps were not further equilibrated. About 15 min were needed to adapt the pressure for each pressure step. The sample was equilibrated for 15 min, when changing the temperature with the pressure cell. Before the first measurement, the sample was equilibrated for 20 min.

In the glass cuvette, the sample was equilibrated for at least 30 min after reaching the desired temperature.

The samples measured with SANS were synthesized in D_2O and measured at a concentration of 50 g/L.

The SANS data was fitted with SasView 3.1.1. This work benefited from the use of the SasView application, originally developed under NSF award DMR-0520547. All the models are convoluted with the instrument resolution function.[6]

The SANS data was recorded at a concentration of 50 g/L. Due to the high concentration the scattered intensity is the product of the form factor, P(q), and the structure factor, S(q). The resulting structure factor for spherical particles is fitted with a Hayter MSA structure factor[7]. Hereby, a constant salt concentration of 0.001 mol/L and a constant SLD of $6.33 \cdot 10^{-6}$ Å^{-2} for D_2O is used. Also, the temperature is fixed to the measurement temperature and the dielectric constant of the D_2O is fixed to the literature value at the according temperature.[8] The models used for the form factor are different, depending on the structure exposed. In case of a core shell fitting model we obtain a SLD for the shell of $5.8 \cdot 10^{-6} \pm 0.3 \cdot 10^{-6}$ Å^{-2} and for a SLD for the core of $1.8 \cdot 10^{-6} \pm 0.5 \cdot 10^{-6}$ Å^{-2}. The error in the following Tables S2-S8 shows the variation of each parameter which will result in an increase of X^2 of 5%.

Hayter MSA Structure Factor[7, 9].

This is an implementation of the Rescaled Mean Spherical Approximation which calculates the structure factor (the Fourier transform of the pair correlation function $g(r)$) for a system of charged, spheroidal objects in a dielectric medium. When combined with an appropriate form

factor (such as sphere, core-shell, ellipsoid, etc.), this allows for inclusion of the interparticle interference effects due to screened coulomb repulsion between charged particles.

Spherical Core-Shell Model[9-10]: Fits for spherical particles with a similar block length of the soluble block and the core-forming block (*DP* = 50 and *DP* = 90).

For spherical particles, which are based on a polymer with a similar block length of the soluble block and the core-forming block (*DP* = 50 and *DP* = 90) we used a spherical core/shell fitting model.[10] The results of the fits with a core-shell model in combination to the Hayter MSA structure factor are summarized in Table S2.

Table S2. Spherical core shell fitting parameter for particles made of DP50 and DP90

	Charge [e]	Radius [nm]	Thickness [nm]	Volume fraction	Distribution Radius
A_{49}-*b*-B_{90}LSC 25°C	44±5	11.4±0.3	5.2±0.3	0.079±0.001	0.236±0.02
A_{49}-*b*-B_{90}LSC 25°C[b]	23±2	8.1±0.3	5.1±0.3	0.111±0.002	0.213±0.02
A_{49}-*b*-B_{90}LSC 15°C 40 bar	36±10	10.5±1	6.5±1	0.084±0.002	0.282±0.05
A_{49}-*b*-B_{90}LSC 15°C 40 bar[b]	19±2	4.9±0.3	6.3±0.3	0.072±0.002	0.291±0.03
A_{49}-*b*-B_{50}LSC 25°C	20±1	6.9±0.3	5.0±0.2	0.126±0.002	0.188±0.01
A_{49}-*b*-B_{50}LSC 25°C[b]	17±2	6.3±0.3	5.0±0.2	0.136±0.001	0.20±0.02

[b] measured after applied trigger

The 1D scattering intensity is calculated in the following way

$$P(q) = \frac{scale}{V_s}\left[3V_c(\rho_c - \rho_s)\frac{[\sin(qr_c) - qr_c\cos(qr_c)]}{(qr_c)^3} + 3V_s(\rho_s - \rho_{solv})\frac{[\sin(qr_s) - qr\cos(qr_s)]}{(qr_s)^3}\right]^2 + bkg$$
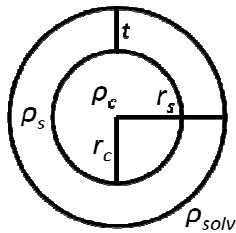
where *scale* is a scale factor, V_s is the volume of the outer shell, V_c is the volume of the core, r_s is the radius of the core+shell, r_c is the radius of the core, t is the thickness of the shell ($t = r_s - r_c$), ρ_c is the scattering length density of the core, ρ_s is the scattering length density of the shell, ρ_{solv} is the scattering length density of the solvent, and *bkg* is the background level

Hard Sphere Model[9-10]: Fits for spherical particles, whose block length of the core forming block is significantly longer than the soluble block (DP = 400).

For spherical particles, whose block length of the core forming block is significantly longer than the soluble block (DP = 400; 8 times longer core forming block than soluble block), we use a hard sphere model[10] as the main contribution to the scattering comes from the core. Further, we do not see an improvement of the fit when using a core-shell model or fuzzy
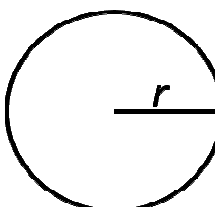
sphere model for these polymers (X^2 does not improve significantly). The results of the fits with a hard sphere model in combination to the Hayter MSA structure factor is summarized in Table S3:

Table S3. Hard sphere fitting parameter for particles made of DP400

	Charge [e]	Radius [nm]	Volume fraction	Distribution of Radius
A_{49}-b-B_{400}HSC 15°C[b]	55±10	9.0±0.1	0.014±0.002	0.35±0.03
A_{49}-b-B_{400}LSC 15°C[b]	58±10	8.5±0.2	0.0096±0.002	0.36±0.01
A_{49}-b-B_{400}LSC 15°C 40 bar[b]	42±10	7.6±0.2	0.011±0.002	0.37±0.02
A_{49}-b-B_{400}HSC 15°C 40 bar[b]	46±10	8.1±0.1	0.013±0.003	0.32±0.03
A_{49}-b-B_{400}LSC 15°C	1112±400	36.7±2	0.046±0.01	0.17±0.04

[b] measured after applied trigger

The 1D scattering intensity is calculated in the following way

$$I(q) = \frac{scale}{V} \cdot \left[\frac{3V(\Delta\rho)(\sin(qr) - qr\cos(qr))}{(qr)^3} \right]^2 + bkg$$

where scale is a volume fraction, V is the volume of the scatterer, r is the radius of the sphere, bkg is the background level and $\Delta\rho$ is the scattering contrast difference between the scatterer and the solvent.
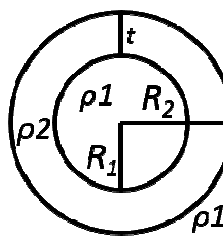
Vesicle Model:[9-10] (Hollow Core-Shell Model) Fits for vesicles.

The vesicles obtained when polymerizing at high concentrations and high DP are fitted with a vesicle form factor (hollow core shell). The fitting parameters are summarized in Table S4:

Table S4. Vesicle model fitting parameter for A_{49}-b-B_{400}HSC before stimulus

	Radius [nm]	Thickness [nm]	Dispersity Radius	Dispersity Thickness
A_{49}-b-B_{400}HSC 25°C	110±20	28.7±2	0.4±0.3	0.3±0.02

The 1D scattering intensity is calculated in the following way

$$P(q) = \frac{scale}{V_{shell}} \left[\frac{3V_1(\rho_1 - \rho_2)J_1(qR_1)}{qR_1} + \frac{3V_2(\rho_2 - \rho_{solv})J_1(qR_2)}{qR_2} \right]^2 + bkg$$

where scale is a scale factor, V_{shell} is the volume of the shell, V_1 is the volume of the core, V_2 is the total volume, R_1 is the radius of the core, R_2 is the outer radius of the shell, ρ_1 is the scattering contrast of the core and the solvent ($\rho_1 = \rho_{solv}$), ρ_2 is the scattering contrast of the shell, *bkg* is the background level, and $J_1 = (\sin x - x \cos x)/ x^2$. The functional form is identical to a "typical" core-shell structure, except that the scattering is normalized by the volume that is contributing to the scattering, namely the volume of the shell alone. Also, the vesicle is best defined in terms of a core radius ($= R_1$) and a shell thickness t ($= R_2 - R_1$)

Cylindrical Model:[9-10] Fits for worm-like micelles.

When observing a q^{-1} dependency at low q, we fit the scattering data with a cylinder form factor. This is the case for A_{49}-*b*-B_{400}LSC and diluted A_{49}-*b*-B_{400}HSC at 25 °C after applying the temperature trigger. In the observed q-range, we do not observe any structure factor for this data. Due to the limited q-range, the length is a pure approximation. The cryo-SEM images and the point, that these gels cannot be diluted, indicate both a formation of an interconnected network by this cylindrical motif. In the observed q-range there is no influence on the scattering by this interconnection. Hence, the used cylindrical model is still valid for the observed q-range. But one should keep in mind, that the observed length is an artifact caused by the limited q-range and the model which is only appropriate for this q-range. For A_{49}-*b*-B_{400} we use a fit model without a shell as discussed for the spherical particle with a *DP* of 400. The fit results are summarized in Table S5.

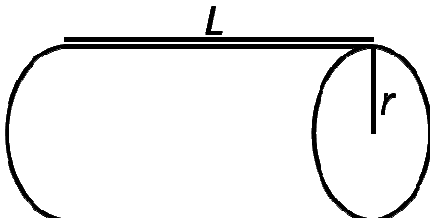**Table S5.** Cylinder model fitting parameter for DP400 at 25°C after temperature stimulus

	Length [nm]	Radius [nm]	Dispersity Radius
A_{49}-*b*-B_{400}LSC 25°C[b]	121±5	8.4±0.2	0.20±0.02
A_{49}-*b*-B_{400}HSC 25°C[b]	114±3	8.5±0.2	0.21±0.02

[b] measured after applied trigger

The output of the 1D scattering intensity function for randomly oriented cylinders is then given by

$$P(q) = \frac{scale}{V} \int_0^{\pi/2} f^2(q, \alpha) \sin \alpha \, d\alpha + bkg$$

where

$$f(q) = 2(\Delta\rho)V \sin(qL \cos \alpha / 2)/(qL \cos \alpha / 2) \frac{J_1(qr \sin \alpha)}{(qr \sin \alpha)}$$

and α is the angle between the axis of the cylinder and the q-vector, V is the volume of the cylinder, L is the length of the cylinder, r is the radius of the cylinder, and $\Delta\rho$ is the scattering contrast difference between the scatterer and the solvent. J_1 is the first order Bessel function.

Combination of Cylindrical and Hard Sphere Model:[9-10] Fits for mixture of worm-like micelles and spherical micelles (*DP* = 400).

After applying the pressure trigger to A_{49}-*b*-B_{400}LSC and diluted A_{49}-*b*-B_{400}HSC followed by heating to 25 °C, we observe at low q a dependency between q^0 and q^{-1}. We assume that due to a shorter waiting time after the pressure trigger, there is still a certain number of spheres present. Not all spherical particles had enough time to aggregate to the cylindrical particles. To account for this effect, we used a combination of a spherical and a cylindrical form factor. The used parameter resembles the ones shown in Table S3 and S5 varying only the scattering contribution of hard spheres and cylinders to obtain an idea about the contribution of spheres and cylinder to the overall scattering. The fit parameters for the combination of a hard sphere and a cylindrical model are summarized in Table S6

Table S6. Combination of hard sphere and cylindrical model fitting parameters for DP400 after pressure trigger and short equilibration at 25°C

	Scale Cyl	Fraction Sph
A_{49}-*b*-B_{400}HSC 40 bar 25°C[b]	0.1151±0.01	0.02246±0.007
A_{49}-*b*-B_{400}LSC 40 bar 25°C[b]	0.063±0.006	0.011±0.004

[b] measured after applied trigger

Cylindrical Core-Shell Model:[9] Fits for worm-like micelles with similar block length of the soluble block and the core-forming block (DP = 90).

The sample A_{49}-*b*-B_{90}HSC is the only exception, where the synthesis was not done in D_2O. For this sample, we diluted the wormlike micelles in D_2O to 5g/L. Again, we need to use a cylindrical core/shell model[11] for these worms, as the core forming block is not significant larger than the soluble block. The worm-like micelles are too long to show a Guinier regime at the observed q-range. The obtained value for the length of the micelles is therefore only a rough approximation. The error on the fit regarding the length of the worm-like structures is caused by the limited q-range. The fit parameters are summarized in Table S7.

Table S7. Cylinder core/shell model fitting parameter for DP90HSCC5

	Length [nm]	Radius [nm]	Thickness [nm]	Dispersity Radius
A_{49}-*b*-B_{90}HSC 25°C	900±300[a]	7.4±0.5	5.0±1	0.16±0.03

[a]The huge error indicates that the observed q-range at low q is not sufficient to reliably measure the lenth of the worm-like micelles.
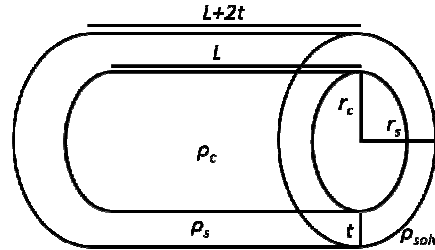
The output of the 1D scattering intensity function for randomly oriented cylinders is then given by

$$P(q) = \frac{scale}{V} \int_0^{\pi/2} f^2(q, \alpha) \sin \alpha \, d\alpha + bkg$$

where

$$f(q) = 2(\rho_c - \rho_s)V_c \sin[qL \cos \alpha/2] / [qL \cos \alpha/2] \frac{J_1[qr \sin \alpha]}{[qr \sin \alpha]}$$

$$+ 2(\rho_s - \rho_{solv})V_s \sin[q(L + 2t) \cos \alpha/2] / [q(L + 2t) \cos \alpha/2] \frac{J_1[q(r+t) \sin \alpha]}{[q(r+t) \sin \alpha]}$$

$$V_s = \pi(R + t)^2 \cdot (L + 2t)$$

and α is the angle between the axis of the cylinder and the q-vector, V_s is the volume of the outer shell (i.e. the total volume, including the shell), V_c is the volume of the core, L is the length of the core, r is the radius of the core, t is the thickness of the shell, ρ_c is the scattering length density of the core, ρ_s is the scattering length density of the shell, ρ_{solv} is the scattering length density of the solvent, and bkg is the background level. The outer radius of the shell is given by $r+t$ and the total length of the outer shell is given by $L+2t$. J_1 is the first order Bessel function.

Gaussian Chain Model:[9, 12] **Fits for dispersed polymer chains.**

The dissolved particles are assumed to form free polymer chains. Therefore, the scattering data for 5 °C or at high pressure are fitted with a Gaussian chain model with a fixed polydispersity (M_w/M_n) of the chains of 1.2. The results are summarized in Table S8.

Table S8. Gaussian chain model parameter

	R_g [nm]
A$_{49}$-b-B$_{90}$LSC 5°C	4.6±0.2
A$_{49}$-b-B$_{50}$LSC 5°C	6.2±0.5
A$_{49}$-b-B$_{400}$LSC 5°C[a]	4.4±0.4
A$_{49}$-b-B$_{400}$HSC 5°C	3.1±0.3
A$_{49}$-b-B$_{90}$LSC 15°C 800 bar	6.5±0.3
A$_{49}$-b-B$_{400}$LSC 15°C 800 bar	8.1±0.4
A$_{49}$-b-B$_{400}$HSC 15°C 800 bar	8.5±0.2

[a] low q can be fitted with hard spheres and a radius of 37 nm.
The scattering intensity $I(q)$ is calculated as

$$I(q) = scale \frac{2[(1 + Ux)^{-1/U} + x - 1]}{(1 + U)x^2} + bkg$$

where *scale* is a scale factor, the dimensionless chain dimension is

$$x = \frac{R_g^2 q^2}{1 + 2U}$$

R_g is the radius of gyration and the polydispersity is

$$U = \frac{M_w}{M_n} - 1.$$

Post mortem morphologies and "phase diagram".

It has previously been shown that the evolution of morphology during RAFT aqueous dispersion polymerization is dependent on both the macro-CTA length and the overall reaction concentration.[1] In all cases, once the hydrophobic block reaches a critical length, primary micelles are formed. The monomer will then partition into the cores, where the polymerization continues. As the chains grow, there are two possible scenarios: (1) At a sufficiently high concentration, inter-particle collisions between spheres will result in the formation of wormlike particles and subsequently vesicles, which can be facilitated by a core-plasticizing effect of free monomer in high concentration. (2) At low concentrations with a long macro-CTA, the micelles will continue to grow, without any evolution in morphology due to the steric repulsion preventing inter-particle collisions required to form worms. These 'kinetically trapped' micelles can also be described as 'crew-cut' micelles.

As a result, all polymer samples exist as spheres at some point during the polymerization, irrespective of the final morphology. In order to understand the possible morphologies achievable using a PDMAM$_{49}$, a "phase diagram" was mapped out based on the morphology observed via post mortem TEM studies conducted on the samples (see Figure S4). It is clear from the images that spheres, worms and vesicles are all accessible by the same chemical pathway.

For such asymmetric amphiphiles, the post mortem diblock copolymer morphology (obtained at nearly full monomer conversion) has a pronounced concentration dependence. Hence, higher order morphologies (i.e., worms or vesicles) can be readily accessed when conducting syntheses at ≥150 g/L solids.

In contrast, spherical micelles can be found for all compositions at lower solid concentrations, e.g. 50 g/L. This concentration dependency was also found for other PISA systems and is probably due to certain kinetic barriers.[1, 13] In addition to the effect of concentration (as observed for different mesophases at various concentrations for low molecular weight surfactants),[14] it is also likely that the high amounts of soluble monomer can have a strong influence due to preferred partitioning and a subsequent plasticizing effect on the insoluble polymer in the particle cores at high monomer concentration. Please note, the polymerization is conducted at temperatures above the melting point of NIPAM monomer (63 °C). Hence, this plasticizing effect facilitates the rearrangement in the insoluble PNIPAM-based domains, which are required to reach their equilibrium structures. In contrast, such a monomer concentration threshold is attained earlier in the polymerization for the dilute samples: the insoluble/non-plasticized (glassy) core-forming component is unable to undergo the structural rearrangements required to perform a morphology transition to higher order structures. These arguments could contribute to the explanation, as it is known that PNIPAM vitrifies (becomes glassy) above a certain temperature (above the LCST) due to continuing exclusion of plasticizing water.[15] This (partial) glass-formation could freeze the structure of the developing crew-cut micelles, which are often regarded as non-equilibrium structures.[16] Finally, the percentage of charged carboxy groups (from the CTA) during dilute synthesis (conducted in pure non-buffered water) is expected to be higher compared to the one at

elevated concentrations. This additionally helps to increase the spatial demands of the water-soluble block and thereby helps to preserve the spherical shape at low synthesis concentrations.

The role of tBAM in this process is twofold: it reduces the transition temperature for the copolymer, and it facilitates vitrification of the insoluble domain by an enhanced exclusion of plasticizing water. That means, the structures get easily frozen upon increasing temperature by tBAM-assisted widening of the temperature regime for the glassy state.

All these factors probably contribute to the directed preparation of non-equilibrium micellar systems.

Figures S1-S13
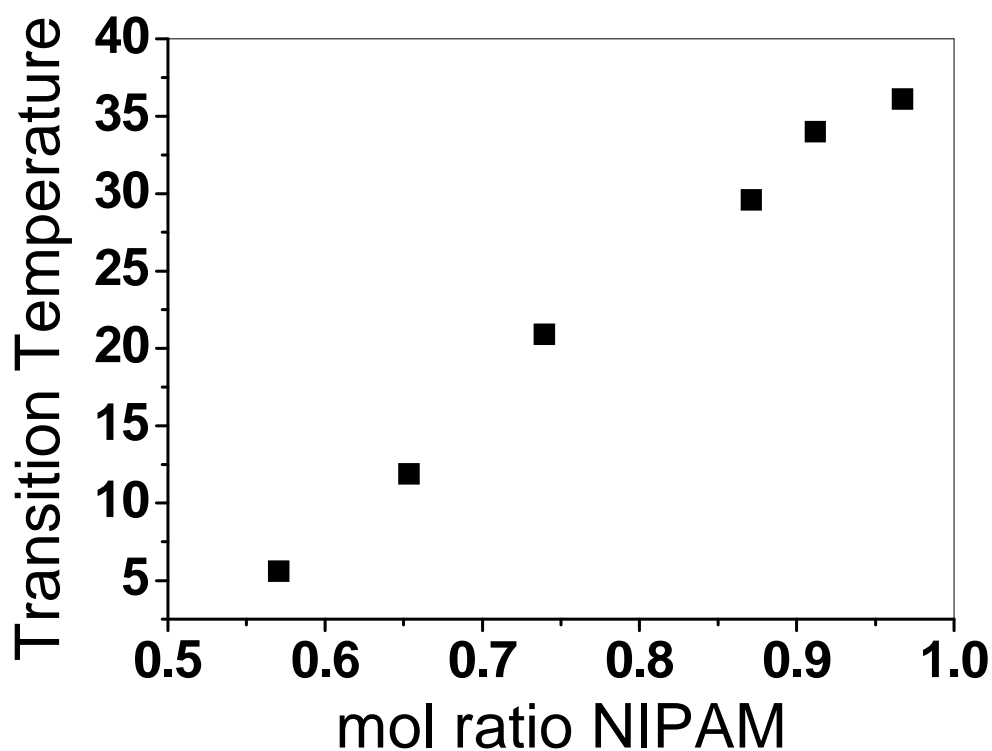
Figure S1. Transition temperature depending on the molar ratio of NIPAM in water. The content of tBAM in a NIPAM chain has a nearly linear effect on the phase separation temperature.[17] The transition temperature is determined at the inflection point of the temperature-dependent intensity of scattered light, measured at 173°. In order to ensure that the core-forming block is collapsed at room temperature but still shows an observable temperature dependency, a tBAM content of 35 mol% in respect to NIPAM content was chosen for all other samples.
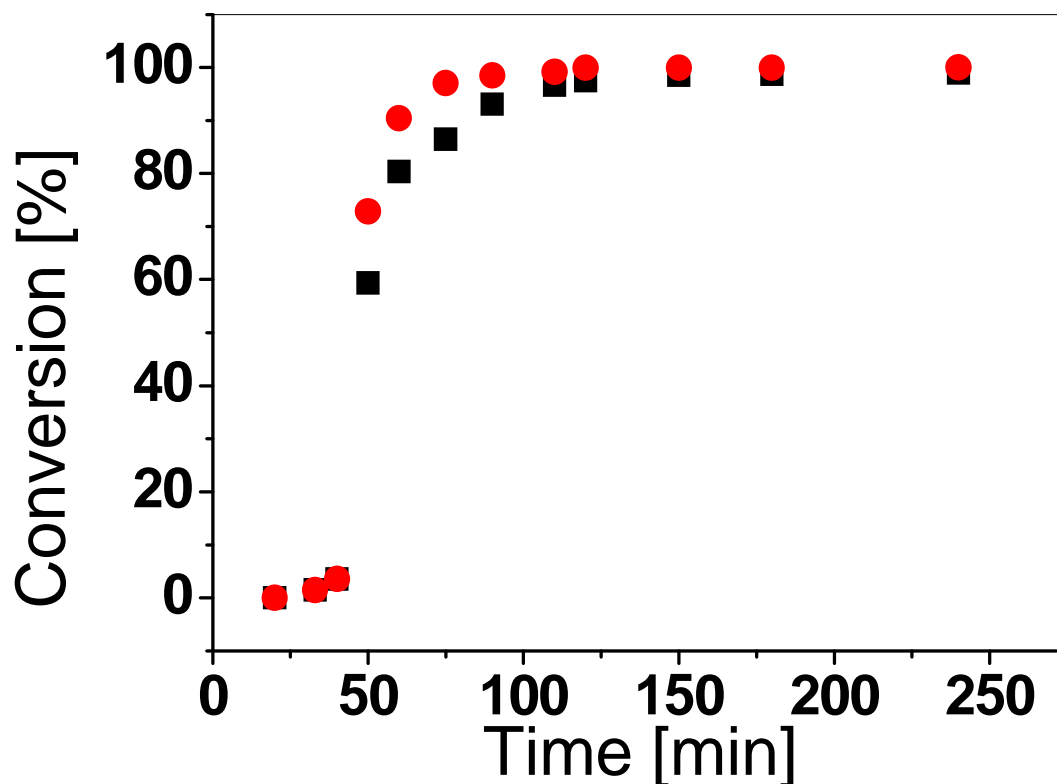
Figure S2. Conversion of the RAFT copolymerization of NIPAM (black) and tBAM (red) at 70 °C in water with an increased macro-CTA to initiator ratio of 10:1 (mol/mol) to reduce the reaction speed. The NIPAM conversion is marked with black squares and the tBAM conversion with red dots. The conversion of this polymerization step was followed by NMR. The conversion is nearly the same for both monomers and therefore we assume a statistical block with a slight gradient. This particular polymerization for kinetic studies was purposely slowed down by reducing the initiator ratio to 1:10 to be able to follow this reaction. The other polymerizations are at high conversions within 30 min but the polymerization is carried out for 2 h to decrease the effect of unconverted monomers.
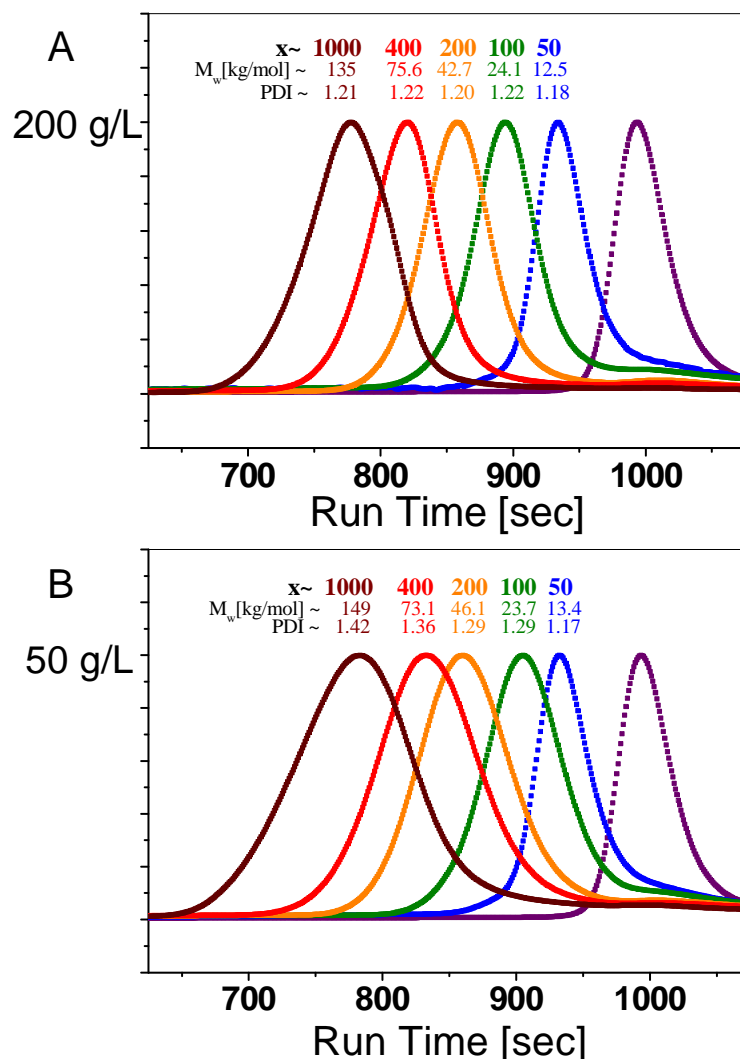
Figure S3. DMF gel permeations chromatograms of exemplary PDMAM$_{49}$-*b*-P(NIPAM-*st*-tBAM)$_{DP}$ diblock copolymers synthesized at 70 °C in aqueous solution with A) 200 g/L solids and B) 50 g/L solids. Degree of polymerization of the core-forming block (as calculated by ^{1}H NMR) is displayed above the elugrams in the according color, the PDMAM$_{49}$ macro-CTA is shown in purple. The GPC traces show still low amounts of macro CTA in the block copolymer samples. For a fixed degree of polymerization (*DP*) of the stabilizer (DMAM) block, systematic variation of the target *DP* of the core-forming (NIPAM-*st*-tBAM) block leads to a monotonic increase in the GPC molecular weight of the diblock copolymer, as expected. Moreover, essentially the same molecular weight distribution is obtained for a given targeted diblock composition, regardless of whether the final diblock copolymer morphology is spheres, worms, or vesicles (or a mixed phase). Using this technique, we are able to synthesize copolymers with a long p(NIPAM-*st*-tBAM) block containing ~1000 repeating units and still achieve a narrow weight distribution.
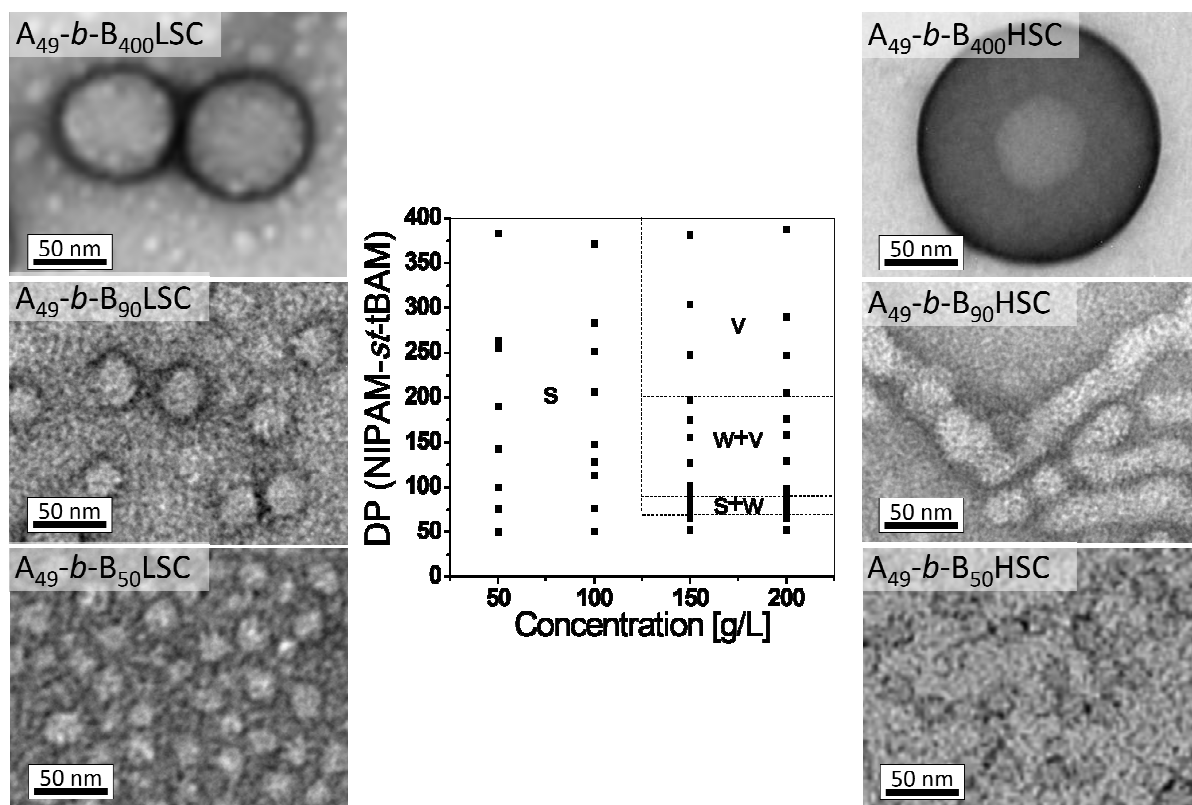
Figure S4. "phase diagram" of PDMAM$_{49}$-b-P(NIPAM-st-tBAM)$_{DP}$ reflecting the micellar morphologies as obtained directly after an aqueous RAFT dispersion polymerization at different solid concentrations ranging from 50 g/L to 200 g/L: S = spherical micelles; W = worm like micelles; V = vesicles. Including TEM images of representative PDMAM$_{49}$-b-P(NIPAM-st-tBAM)$_{DP}$ nanoparticles obtained with increasing final DP of the core-forming P(NIPAM-st-tBAM)$_{DP}$ block.
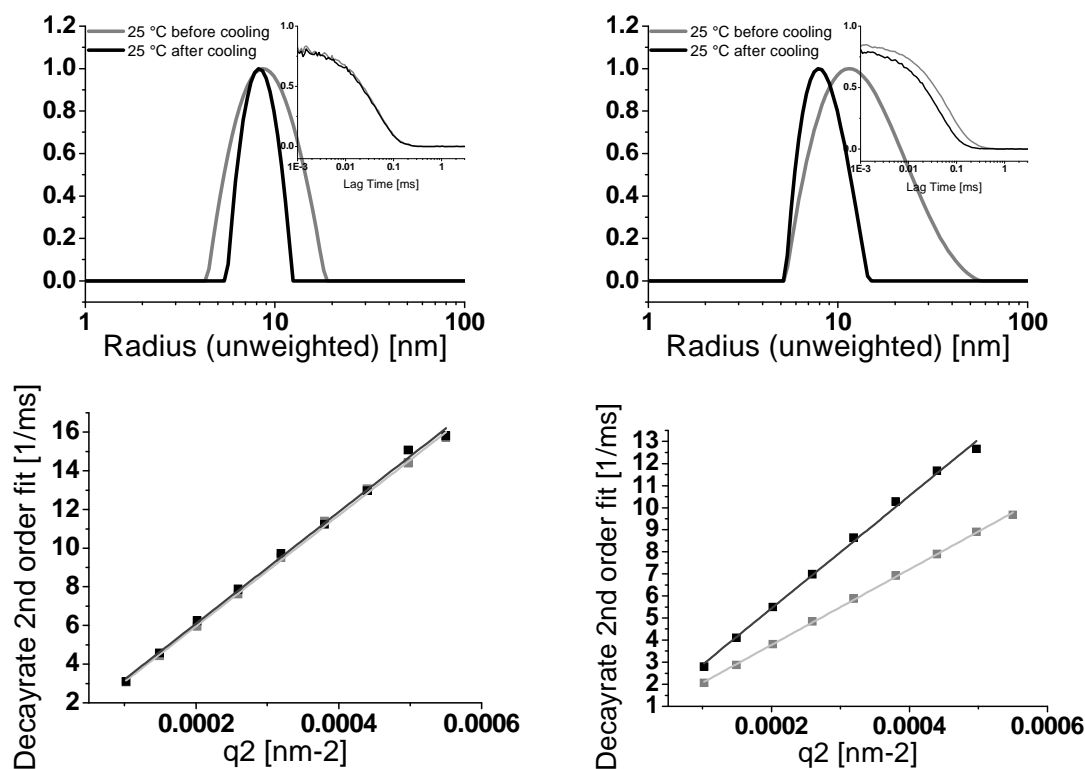
Figure S5. DLS data at 25 °C on reversible and irreversible sphere to sphere transition. A) CONTIN analyses of the autocorrelation shown in the inlet (recorded at 95°) of A_{49}-b-B_{50}LSC before cooling (grey line) and after cooling (black line). Differences in the width can be accounted to the slightly higher noise in the autocorrelation function. B) Decay rate of the 2nd order cumulant fit against q^2 of A_{49}-b-B_{50}LSC leading to a hydrodynamic radius of 8.5 ± 0.1 nm before cooling (grey symbols and light grey fit line) and to a hydrodynamic radius of 8.4 ± 0.1 nm after cooling (black symbols and dark grey fit line). C) CONTIN analyses of the autocorrelation shown in the inlet (recorded at 95°) of A_{49}-b-B_{90}LSC before cooling (grey line) and after cooling (black line). D) Decay rate of the 2nd order cumulant fit against q^2 of A_{49}-b-B_{90}LSC leading to a hydrodynamic radius of 13.2 ± 0.2 nm before cooling (grey symbols and light grey fit line) and to a hydrodynamic radius of 9.3 ± 0.2 nm after cooling (black symbols and dark grey fit line).
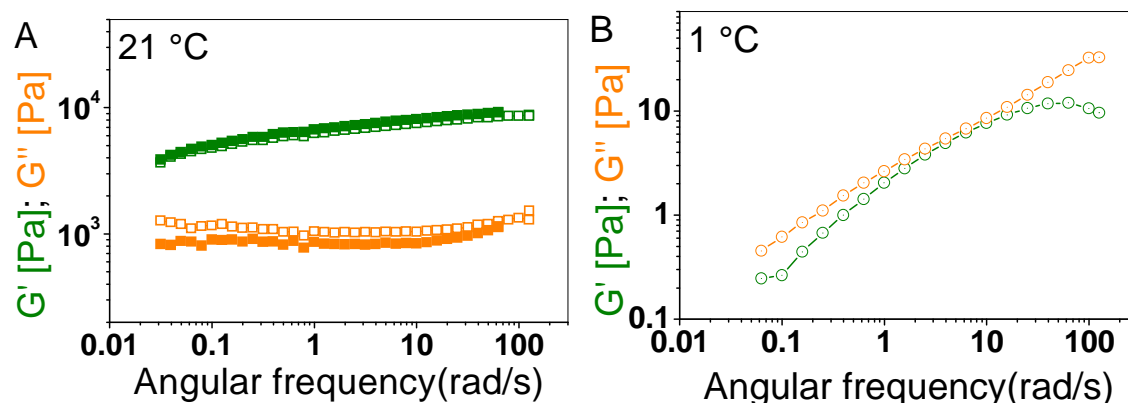
Figure S6. The temperature dependency is tested for A$_{49}$-*b*-B$_{90}$HSC which forms a strong freestanding gel at room temperature. Variation in G' green symbols) and G" (orange symbol). A) frequency sweeps conducted at a strain of 0.5 % and 21°C before cooling and heating cycle (hollow squares) and after cooling and heating cycle (filled squares). The storage modulus exceeds the loss modulus over all measured frequencies showing that the sample behaves like a gel. The storage modulus is at this temperature at ~ 6000 Pa and the loss modulus is nearly one magnitude lower at about ~1000 Pa. The rheological properties are fully restored after cooling and heating cycle.
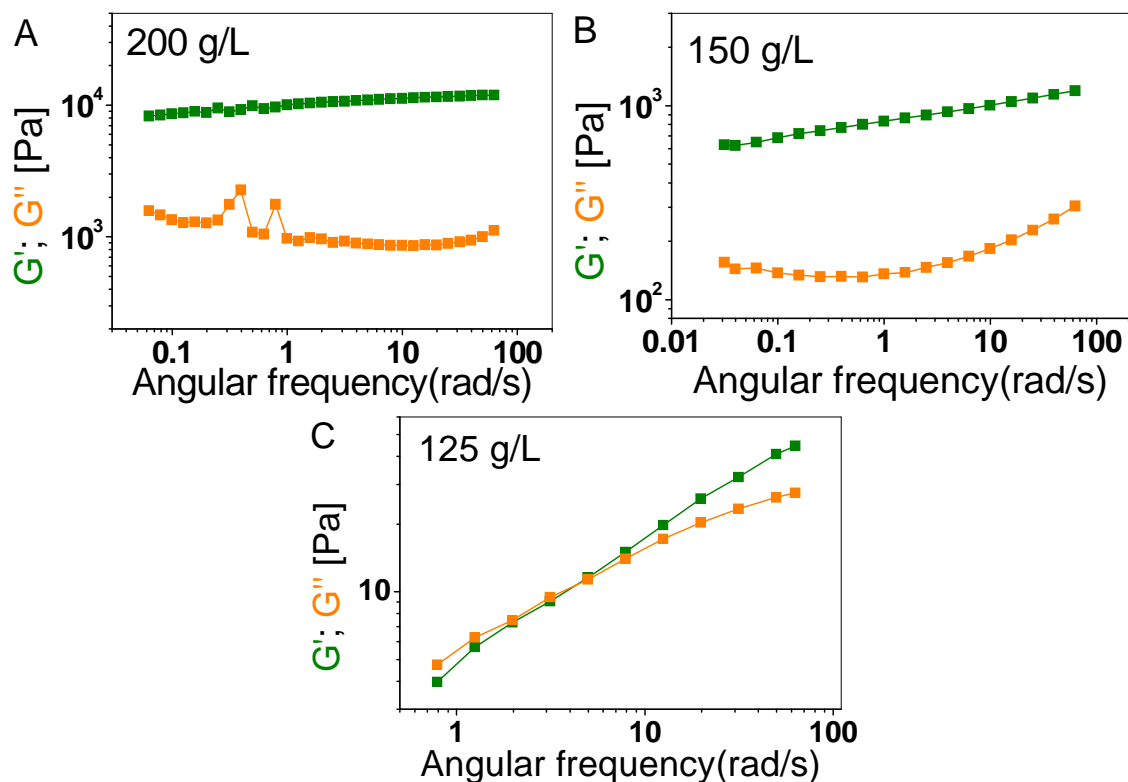B) frequency sweep at a strain of 0.5 % and 1 °C after cooling.

Figure S7. Concentration dependency of the reversible worm-like micelles (A$_{49}$-*b*-B$_{90}$HSC). Frequency sweeps conducted at a strain of 1 % (after LEVR detection) at 21°C for all measurements: G' (green) and G'' (orange). Samples are diluted (where necessary) and loaded at 1°C and then heated to 21°C and equilibrated for 45 min. A) sample concentrated with 200 g/L (concentration of synthesis; G'>G''). B) sample concentrated with 150 g/L (G'>G''). C) sample concentrated with 125 g/L (crossover of G' and G'') When the sample is diluted from 200 g/L to 150 g/L one can see a drastic decrease of G' and G'' of about an order of magnitude while G' still exceeds the G'' over all measured frequencies. The behavior changes drastically, when the sample is diluted to 125 g/L. For this sample, G' exceeds G'' only at high frequencies. At low frequencies G'' exceeds G' and the sample reacts like a liquid. The crossover is at ~ 4 rad/s. This drastic change indicates that there are no entangled wormlike micelles in the sample.
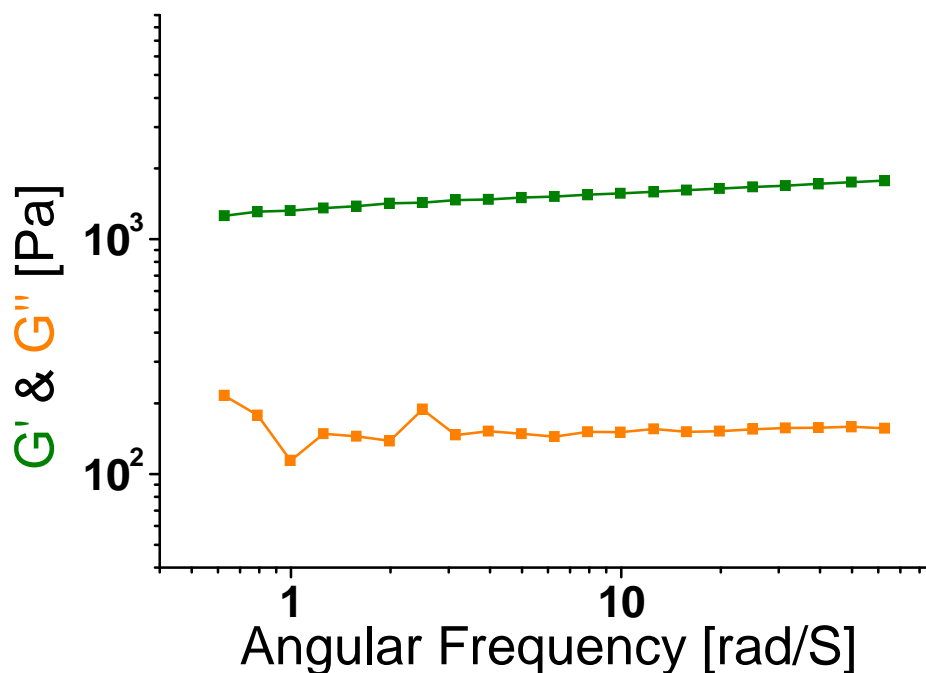
Figure S8. Frequency sweep to demonstrate the reversible gelation of A$_{49}$-b-B$_{90}$ at solid concentrations of 200 g/L. A$_{49}$-b-B$_{90}$LSC (crew cut micelles after polymerization) was freeze dried and dissolved at low temperature at a concentration of 200 g/L leading to a similar concentration as for A$_{49}$-b-B$_{90}$HSC. Frequency sweeps conducted at a strain of 0.2 % (after LEVR detection) at 21°C for all measurements: G' (green) and G" (orange). Upon heating the concentrated A$_{49}$-b-B$_{90}$LSC formed a gel with rheological properties similar to A$_{49}$-b-B$_{90}$HSC. The differences in the properties probably originates in slight differences in the actual polymer and in differences in the polymer concentration (the solid concentration of A$_{49}$-b-B$_{90}$HSC might be slightly higher due to evaporation during purging with N$_2$ before the synthesis).
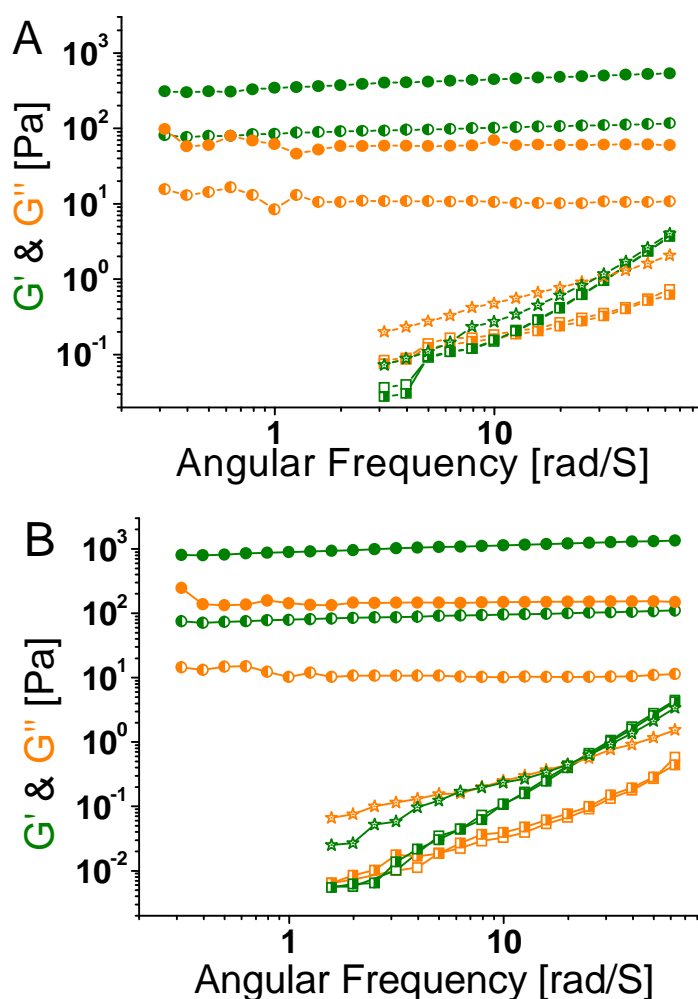
Figure S9. Frequency sweeps showing the transition from crew-cut/vesicular micelles to dispersed chains to small spheres (colloidal gel) to worm-like micelles. Frequency sweeps are conducted at a strain of 0.5 % (after LVER detection) at different temperatures: at 25°C before cooling hollow squares, 15°C before cooling half-filled squares, 1°C stars, 15°C after cooling half-filled circles, 25°C after cooling filled circles for all measurements: G' (green symbols) and G'' (orange symbol). A) A_{49}-*b*-B_{400}LSC crew cut micelles before application of trigger B) A_{49}-*b*-B_{400}HSC vesicles diluted to LSC before application of trigger. The crew-cut/vesicular micelles show the behavior of a viscoelastic liquid at all temperatures before the transition temperature (25°C and 15°C; with a crossover of G' and G'' at ~12 rad/s for A_{49}-*b*-B_{400}LSC and ~3 rad/s for diluted A_{49}-*b*-B_{400}HSC). Below the transition temperature to a viscoelastic (1°C; with a shifted crossover of G' and G'' at ~30 rad/s for A_{49}-*b*-B_{400}LSC and ~20 rad/s for diluted A_{49}-*b*-B_{400}HSC) to a colloidal gel, where G' exceeds G'' at all investigated frequencies at 15°C and finally to an interconnected gel, where G' exceeds G'' at all investigated frequencies at 25°C. The temperature dependent measurement at 1 Hz, is shown in the main article (Figure 2E for A_{49}-*b*-B_{400}LSC and Figure 2I for diluted A_{49}-*b*-B_{400}LSC) and for two cycles in Figure S10.
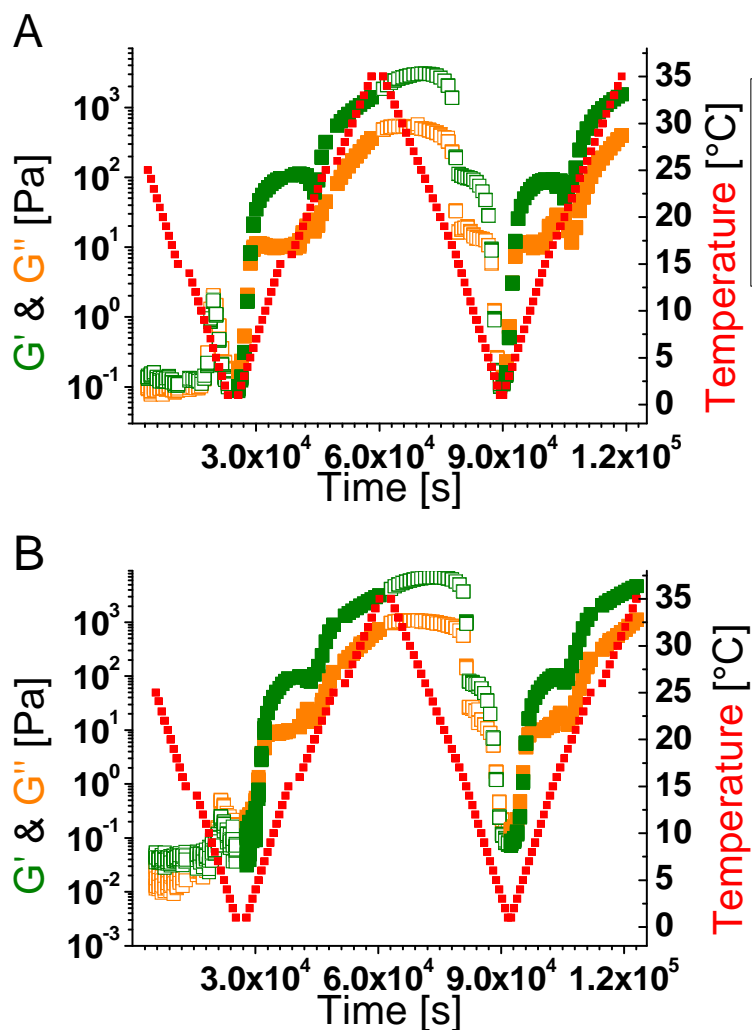
Figure S10. Temperature dependent elastic (G' green) and viscous (G'' orange) moduli recorded at 1 Hz during two temperature cycles (hollow symbols cooling, solid symbols heating). The corresponding temperature is shown with red symbols. The second temperature cycle shows that the worm - dispersed polymer chains - worm transition is reversible. A) crew-cut micelles A_{49}-b-B_{400}LSC B) diluted A_{49}-b-B_{400}HSC vesicles.
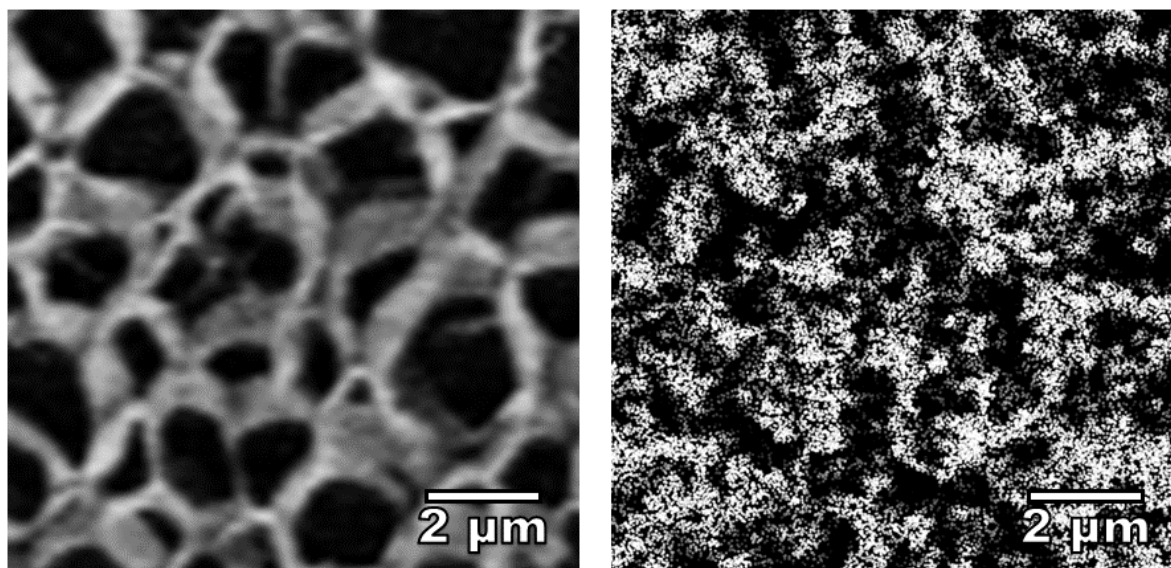
Figure S11. Left: cryo-SEM of A$_{49}$-*b*-B$_{400}$-LSC after applied temperature trigger; Right: Superresolution Fluoresence Microscopy image obtained under dSTORM conditions. The porous structure seen in cryo-SEM is also observed in the superresolved fluorescence microscopy images *in situ*. The more pronounced pore structure in the cryo-SEM image might be explained by a partial collapse and bundling of the interconnected micellar structure during sublimation of water in the cryo-SEM.
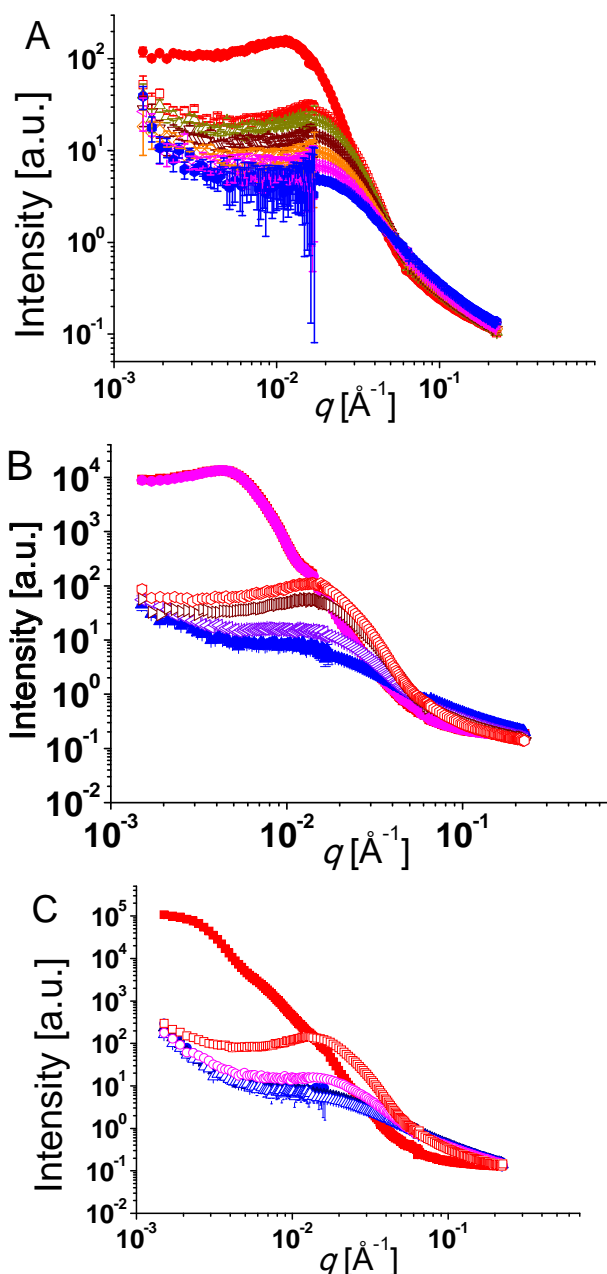
Figure S12. Hydrostatic pressure at a constant temperature of 15°C as stimulus for demicellization and as trigger for irreversible structure changes: A) SANS measurements of small crew cut micelle A_{49}-b-B_{90}LSC. B) SANS measurements of large crew cut micelle A_{49}-b-B_{400}LSC. C) SANS measurements of vesicles diluted A_{49}-b-B_{400}HSC. SANS data at different pressures (and temperatures) before (full symbols) and after pressure trigger (hollow symbols). Ambient pressure red, 100 bar brown, 200 bar dark yellow, 300 bar orange,400 bar, magenta, 500 bar purple, 800 bar blue (1000 bar for A_{49}-b-B_{400}LSC), 1200 bar dark blue. All measurements at 50 g/L.
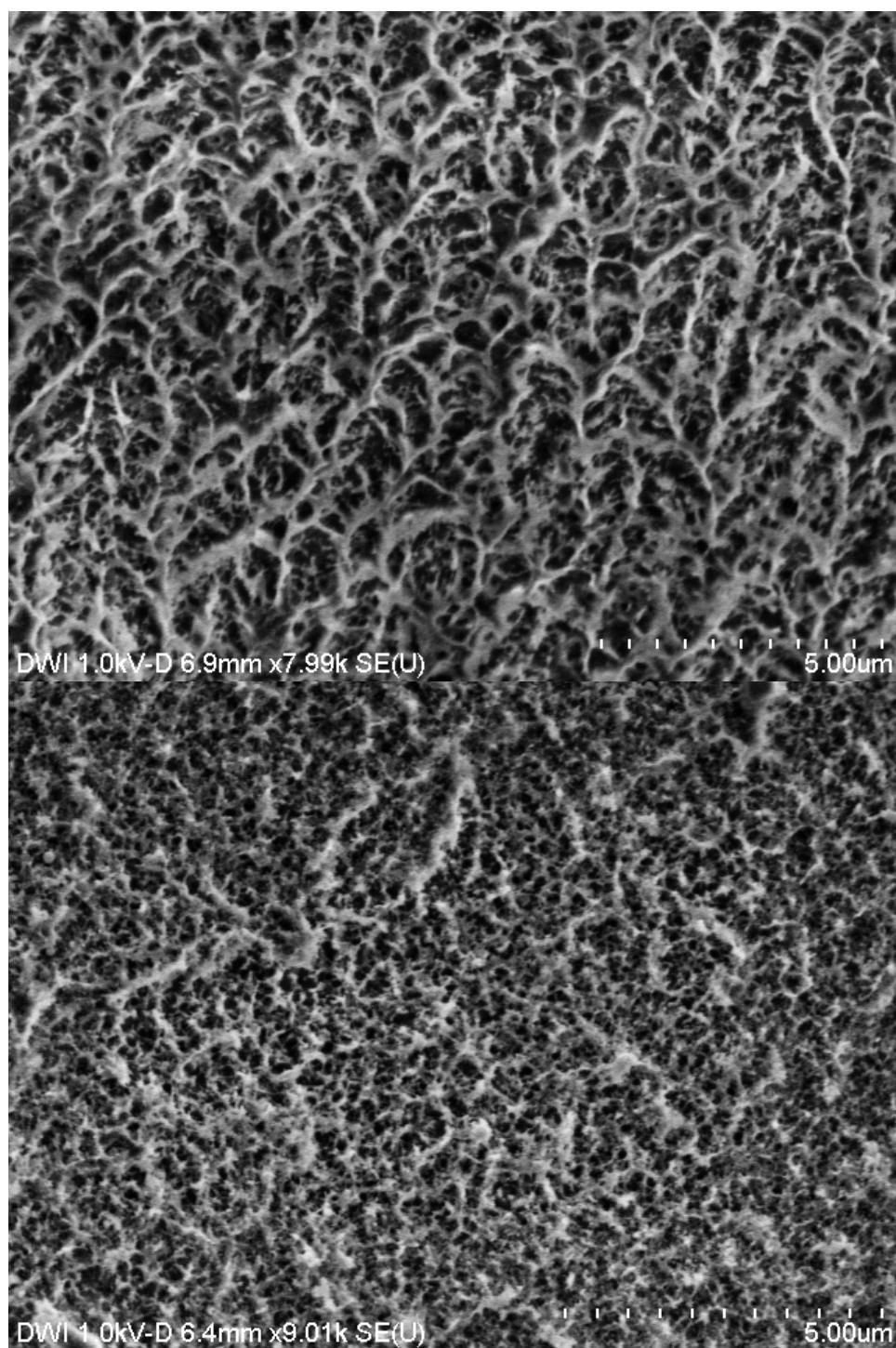
Figure S13. Cryo-SEM image obtained for the A$_{49}$-*b*-B$_{400}$LSC gel (upper picture) and for the A$_{49}$-*b*-B$_{400}$LSC gel (lower picture) when returned to 25 °C after the pressure trigger.

References

[1] A. Blanazs, A. J. Ryan, S. P. Armes, *Macromolecules* **2012**, *45*, 5099-5107.

[2] aM. Heilemann, S. van de Linde, M. Schüttpelz, R. Kasper, B. Seefeldt, A. Mukherjee, P. Tinnefeld, M. Sauer, *Angew. Chem. Int. Ed.* **2008**, *47*, 6172-6176; bS. van de Linde, R. Kasper, M. Heilemann, M. Sauer, *Appl. Phys. B: Lasers Opt.* **2008**, *93*, 725-731.

[3] M. Ovesny, P. Krizek, J. Borkovec, Z. Svindrych, G. M. Hagen, *Bioinformatics* **2014**, *30*, 2389-2390.

[4] M. El Beheiry, M. Dahan, *Nat. Methods* **2013**, *10*, 689-690.

[5] A. Steinschulte, S. Bochenek, F. Plamper, S. Schneider, R. Schweins, A. Scotti, N. Warren, R. Winter, *Institut Laue-Langevin (ILL)* **2016**.

[6] J. S. Pedersen, D. Posselt, K. Mortensen, *J. Appl. Crystallogr.* **1990**, *23*, 321-333.

[7] aJ. P. Hansen, J. B. Hayter, *Mol. Phys.* **1982**, *46*, 651-656; bJ. B. Hayter, J. Penfold, *Mol. Phys.* **1981**, *42*, 109-118.

[8] C. G. Malmberg, *J. Res. Natl. Bur. Stand.* **1958**, *60*, 609-612;Research Paper 2874.

[9] http://www.sasview.org/.

[10] A. Guinier, G. Fournet, *Small-Angle Scattering of X-rays*, John Wiley & Sons, **1955**.

[11] I. Livsey, *J. Chem. Soc. Farad. T. 2* **1987**, *83*, 1445-1452.

[12] O. Glatter, O. Kratky, Editors, *Small Angle X-ray Scattering*, Academic Press, **1982**.

[13] S. Sugihara, A. Blanazs, S. P. Armes, A. J. Ryan, A. L. Lewis, *Journal of the American Chemical Society* **2011**, *133*, 15707-15713.

[14] D. J. Mitchell, G. J. T. Tiddy, L. Waring, T. Bostock, M. P. McDonald, *Journal of the Chemical Society, Faraday Transactions 1: Physical Chemistry in Condensed Phases* **1983**, *79*, 975-1000.

[15] V. O. Aseyev, H. Tenhu, F. M. Winnik, in *Conformation-Dependent Design of Sequences in Copolymers II* (Ed.: A. R. Khokhlov), Springer Berlin Heidelberg, Berlin, Heidelberg, **2006**, pp. 1-85.

[16] O. V. Borisov, E. B. Zhulina, F. A. M. Leermakers, A. H. E. Müller, in *Self Organized Nanostructures of Amphiphilic Block Copolymers I* (Eds.: E. A. H. Müller, O. Borisov), Springer Berlin Heidelberg, Berlin, Heidelberg, **2011**, pp. 57-129.

[17] aJ. D. Debord, L. A. Lyon, *Langmuir* **2003**, *19*, 7662-7664; bA. S. Hoffman, P. S. Stayton, V. Bulmus, G. Chen, J. Chen, C. Cheung, A. Chilkoti, Z. Ding, L. Dong, R. Fong, C. A. Lackey, C. J. Long, M. Miura, J. E. Morris, N. Murthy, Y. Nabeshima, T. G. Park, O. W. Press, T. Shimoboji, S. Shoemaker, H. J. Yang, N. Monji, R. C. Nowinski, C. A. Cole, J. H. Priest, J. Milton Harris, K. Nakamae, T. Nishino, T. Miyata, *J. Biomed. Mater. Res.* **2000**, *52*, 577-586.